



# Automated water content reconstruction of zero-offset borehole ground penetrating radar data using simulated annealing

Dale F. Rucker\*, Ty P.A. Ferré

*Department of Hydrology and Water Resources, University of Arizona, P.O. Box 210110, Tucson, AZ 85721, USA*

Received 29 October 2003; revised 15 October 2004; accepted 9 November 2004

## Abstract

The automated inversion of water content profiles from first arrival travel time data collected with zero-offset borehole ground penetrating radar is discussed. The inversion algorithm sets out to find the water content profile that minimizes a least-squares objective function representing the difference between the modeled and measured first arrival travel time. Ray-tracing analysis is used to determine the travel time for direct and critically refracted paths to identify the first arrival travel time. This automated method offers improvement over a previously presented graphical solution that considers both direct and critical refractions. Specifically, this approach can identify thinner layers and allow for the incorporation of uncertainty in the travel time measurements to determine the depth-specific uncertainty of the inferred water content profile through multiple simulations using a stochastic approach.

© 2004 Elsevier B.V. All rights reserved.

*Keywords:* Borehole ground penetrating radar; Water content; Uncertainty; Monte Carlo; Simulated annealing; Optimization

## 1. Introduction

Measuring the relative apparent dielectric permittivity of moist soil is an attractive and cost efficient method to indirectly acquire the soil's volumetric water content. Two geophysical tools are commonly used to obtain the permittivity: time domain reflectometry (TDR) and ground penetrating radar (GPR). Both tools measure the travel time of a propagating electromagnetic (EM) wave, which can be related

directly to the volumetric water content (Topp et al., 1980). TDR uses parallel wave guides to direct the waves through the soil under investigation. Reflections of the EM wave occur at boundaries of contrasting permittivity and at the end of the wave guides. The two-way travel time of the guided wave is then obtained with an oscilloscope. GPR emits a pulse from a transmitting antenna, which undergoes spherical spreading through the subsurface (Davis and Annan, 1989). A receiving antenna records the pulses that travel through direct and indirect routes between the antennae. The electromagnetic energy is recorded as a radargram (Cai and McMechan, 1995), which is similar to a seismogram recording of acoustic energy. In cross borehole GPR applications, the travel time at

\* Corresponding author. Address: 8240 E. Pima Street, Tucson, AZ 85715, USA

E-mail addresses: [druck@hwr.arizona.edu](mailto:druck@hwr.arizona.edu) (D.F. Rucker), [ty@hwr.arizona.edu](mailto:ty@hwr.arizona.edu) (T.P.A. Ferré).

each measurement depth is evaluated from the first arriving energy on the radargram.

The relative apparent dielectric permittivity ( $K_a$ ) is the square of the ratio of the EM velocity in air ( $0.3 \text{ m ns}^{-1}$ ) to that in a soil (Topp et al., 1980).  $K_a^{0.5}$  can be related to volumetric water content through empirical relations (Topp et al., 1980; Ferré et al., 1996), semi-empirical relations such as geometric models (Feng and Sen, 1985; Friedman, 1998), statistical models (Friedman, 1997), and theoretical models (Tabbagh et al., 2000). For TDR, the propagating EM wave travels directly along the axis of the wave guides over a known path. Therefore, the EM velocity is simply the two-way path length divided by the two-way travel time. The inversion of GPR travel time, however, is ill-posed and non-linear because the travel path is not well defined. An unguided EM wave will interact with the subsurface in several ways simultaneously. Changes in dielectric permittivity throughout the subsurface can cause reflected, refracted, and diffracted waves. These waves arrive at the receiving antenna at times that depend on the individual path lengths and velocity distributions traversed.

The solution of non-linear inverse problems can be obtained by solving the forward model over a range of unknown parameter values until an objective function is minimized. The parameter space is searched until an optimal set of parameters is found. The success of local search methods, such as maximum likelihood (Carrera and Neuman, 1986), relies on a good initial estimate (Boschetti et al., 1996). Global search methods, such as genetic algorithms or simulated annealing are better suited to solve many geophysical problems because they do not rely on gradients of the solution space and their success does not depend on the starting point of any model. However, global search methods are often computationally more expensive (Mosegaard and Vestergaard, 1991) than local search methods.

Many inverse problems are both ill-posed and ill-conditioned. Ill-posedness exists because there are too many unknown parameters in relation to the number of measurements. Specifically for ZOP BGPR, the number of unknowns outnumber the measurements by a factor of two and include the EM propagation velocity within a discrete layer and the boundary location between the layers. Ill-conditioning arises

because the estimated parameters are overly sensitive to the uncertainty in the measured data. A small error in data may cause the solution to vary over a wide range. The success of inversion, therefore, depends greatly on the accurate measurement of the data. Most geophysical methods have inherent measurement uncertainties. For GPR, uncertainty can exist in the measured arrival travel time from random instrumentation and human error.

Rucker and Ferré (2003, 2004a) have investigated the effects of critically refracted arrivals during the inversion of the first arrival time of EM waves using zero-offset profiling (ZOP) with cross-borehole GPR (BGPR). Traditionally, BGPR travel time inversion assumed that all waves travel directly from the transmitter to the receiver (see Davis and Annan (2003), esp. Fig. 3.1.3.5-15). Since the separation distance of the antennae is known, the velocity is obtained by dividing this distance by the travel time of the first arriving energy on the radargram. The assumption of a directly travelling wave is valid when sharp boundaries of dielectric permittivity do not exist. Where they do exist, such as at the ground surface, near the water table, or at a wetting front, critically refracted waves may be the first to arrive. Under these conditions, accurate inversion of the water content profile requires the simultaneous interpretation of many measurements made at various vertical distances from the boundary.

Rucker and Ferré (2003) inverted travel time profiles by using least-squares regression to find the slope of regions with linearly increasing or decreasing travel time. Although this method was shown to be effective for determining the water content in regions affected by critical refraction, the task of hand-fitting the slopes is time consuming especially if large data sets have been collected. In this study, we develop an automated method of reconstructing the velocity profile through the global search optimization technique of simulated annealing. To quantify water content uncertainty due to travel time measurement errors we use stochastic parameter estimation using the Monte Carlo method (e.g. Feyen et al., 2001; Vassolo et al., 1998). To overcome the ill-posedness of the inverse problem, we use regularization through a smoothing constraint that minimizes the first or second derivative of the water content profile (e.g. Tikhonov and Arsenin, 1977). Successful automated

inversion is achieved by meeting four objectives: (1) formulate the inverse problem of ZOP BGPR for water content profiling; (2) demonstrate a method by which a simulated annealing algorithm can be used to solve the ZOP BGPR inverse problem; (3) determine the effects of measurement error on the uncertainty of the estimated parameters; and (4) demonstrate how the simulated annealing algorithm can be used to quantify the uncertainty of experimental data.

## 2. Theory

### 2.1. Raypaths

Direct and critically refracted travel paths are important for the interpretation of ZOP BGPR travel times (Rucker and Ferré, 2003). The travel time of a direct wave is:

$$t_{\text{direct}} = \frac{x}{v}, \quad (1)$$

where  $v$  is the velocity of propagation and  $x$  is the antennae separation distance (Fig. 1). The travel time of a critically refracted wave is:

$$t_{\text{refr}} = \frac{x}{v_{\text{high}}} + z \left[ \frac{2}{v_{\text{low}} \cos \theta_c} - \frac{2 \tan \theta_c}{v_{\text{high}}} \right], \quad (2)$$

where  $v_{\text{low}}$  is a low velocity layer adjacent to a relatively high velocity layer,  $v_{\text{high}}$ . The angle of critical refraction,  $\theta_c$ , is:

$$\theta_c = \sin^{-1} \left[ \frac{v_{\text{low}}}{v_{\text{high}}} \right]. \quad (3)$$

Typically, ZOP velocity calculations are based on the measured travel time of the first arriving energy.

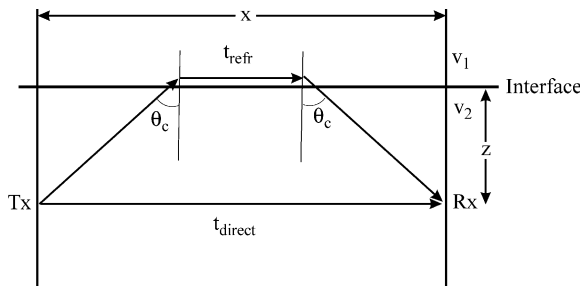


Fig. 1. Ray tracing of the direct and the critically refracted waves near a boundary between two velocity layers, where  $v_1 > v_2$ .

If the antennae are placed within a low velocity layer near a boundary with a higher low velocity layer, the critically refracted wave may arrive first. Specifically, if the distance from the boundary,  $z$ , is equal to the refraction termination depth (Rucker and Ferré, 2003),  $z_{\text{rtid}}$ , the direct travel time will equal the critically refracted travel time. If  $z$  is less than  $z_{\text{rtid}}$ , the critically refracted wave will be the first to arrive.

When interpreting a radar velocity profile, both the locations of boundaries and the layer velocities are unknown. As a result, unique inversion of Eq. (2) to determine  $v_{\text{low}}$  is impossible. To overcome this ill-posedness for their graphical inverse solution, Rucker and Ferré (2003, 2004a) assumed that any boundaries were located at a depth coincident with a measurement location. For thick low-velocity layers, usually greater than 1 m, this assumption will not cause large errors in the graphical solution. However, for thin low velocity layers, especially when the thickness approaches twice the sampling resolution (a.k.a. the Nyquist frequency), the errors in interpreted water content can become quite large (Rucker and Ferré, 2003).

### 2.2. Forward model

Consider a simple half-space with a boundary at the earth's surface and a soil with an EM velocity of  $v_2$ . Two first arrival travel time measurements are made: one above ground (in air) and the other below ground. The velocity in air is larger than the velocity in soil, so no critical refraction will occur when a signal is transmitted in air. When a measurement is made beneath the ground surface, two travel paths are possible: direct and critically refracted (Fig. 1). The two travel time measurements can be described in terms of a general model:

$$\mathbf{Gm} = \mathbf{d}, \quad (4)$$

where the matrix  $\mathbf{G}$  is the data kernel, the vector  $\mathbf{m}$  contains the model parameters, and the vector  $\mathbf{d}$  contains the measured data.  $\mathbf{G}$  represents the constant coefficients that transform model space to data space and is analogous to the Green's function (Menke, 1989). For this example, the model parameters represent the slowness (inverse velocity) of each layer and data parameters represent the first arrival times. If both measurements of travel time are a result

of direct arrivals, then the forward model of travel time is:

$$\begin{bmatrix} x & 0 \\ 0 & x \end{bmatrix} \begin{Bmatrix} s_1 \\ s_2 \end{Bmatrix} = \begin{Bmatrix} t_{d1} \\ t_{d2} \end{Bmatrix}, \quad (5)$$

where  $s_1$  and  $s_2$  are the slowness values and  $t_{d1}$  and  $t_{d2}$  are direct travel times through air and soil, respectively. The matrix  $\mathbf{G}$  is filled along the rows with the antennae separation, such that the first row is multiplied by the slowness values to yield the direct travel time. The second possibility is a direct first arrival in air and critically refracted first arrival below ground. Rewriting Eq. (2) in terms of slowness yields:

$$t_{\text{refr}} = xs_1 + 2za_{1-2}, \quad (6)$$

where

$$a_{1-2} = \sqrt{s_2^2 - s_1^2}. \quad (7)$$

The second possible forward model may be written as:

$$\begin{bmatrix} x & 0 \\ 0 & 2z \end{bmatrix} \begin{Bmatrix} s_1 \\ a_{1-2} \end{Bmatrix} = \begin{Bmatrix} t_{d1} \\ t_{\text{refr}1-2} \end{Bmatrix}, \quad (8)$$

where  $t_{\text{refr}1-2}$  is the travel time of the critically refracted energy at the ground surface. Combining the travel time measurements into a time matrix,  $\mathbf{T}$ , where each column represents a possible travel time profile gives:

$$\mathbf{T} = \begin{bmatrix} t_{d1} & t_{d1} \\ t_{d2} & t_{\text{refr}1-2} \end{bmatrix}. \quad (9)$$

The minimum travel time of each row represents the first arrival travel time at that depth. Collecting these travel times as a vector,  $\mathbf{t}$ , defines the first arrival travel profile. This corresponds with the travel time profile that would be measured from a radargram. As an example, consider a soil with a velocity of  $0.1 \text{ m ns}^{-1}$ , antennae separation of 3 m, and two ZOP BGPR measurements: one in air and one at a depth of 0.5 m below the ground surface.  $\mathbf{T}$  would be populated as follows:

$$\mathbf{T} = \begin{bmatrix} 10 & 10 \\ 30 & 19.428 \end{bmatrix}. \quad (10)$$

The first arrival travel time profile would be  $\mathbf{t} = \{10 \text{ } 19.428\}^T$ . That is, a direct arrival is first to arrive above ground and a critically refracted wave arrives first below ground. For a three-layered geometry with the top layer being air and  $v_3 < v_2$ , five possible outcomes would exist and  $\mathbf{T}$  would be a  $(3 \times 5)$  matrix. Absent from the time matrix are reflections, because it can be shown by geometrical considerations that they will never be first arriving for ZOP BGPR.

### 2.3. Model sensitivity

To demonstrate the errors that can arise during travel time picking, two radar traces are shown (Fig. 2). There is no accepted correct method to determine the absolute first arrival from a GPR trace. One method, which is commonly used in automated picking software (e.g. PICKER by Sensors and Software, Mississauga, Canada) identifies the time at which the amplitude exceeds 5% of the amplitude at the first peak. A second method, is based on identifying the time at which the trace deviates from a constant amplitude; this describes most manual picking methods. Fig. 2A and B includes gray boxes that cover the range of travel times spanning from the earlier time picks that are representative of manual picks and the later times associated with automated picks. As expected, the range of picks is larger for traces containing more high frequency noise (Fig. 2A). However, even noise-free traces (Fig. 2B) give rise to uncertain travel time picks.

To demonstrate how travel time measurements are related to difference in interpreted water contents, we use the empirical model of Ferré et al. (1996) to convert EM velocity in soil to water content,  $\theta$ :

$$\theta = 0.1181 \frac{v_{\text{air}}}{v_{\text{soil}}} - 0.1841. \quad (11)$$

From Eq. (1), assuming a direct arrival and antennae separation of 3.25 m, the first-break pick range in Fig. 2A (29.2–33.8 ns) gives rise to volumetric water content estimates ranging from 0.133 to  $0.184 \text{ cm}^3 \text{ cm}^{-3}$ . If, however, the first arrival is associated with a critical refraction at the ground surface, the soil velocity is defined based on

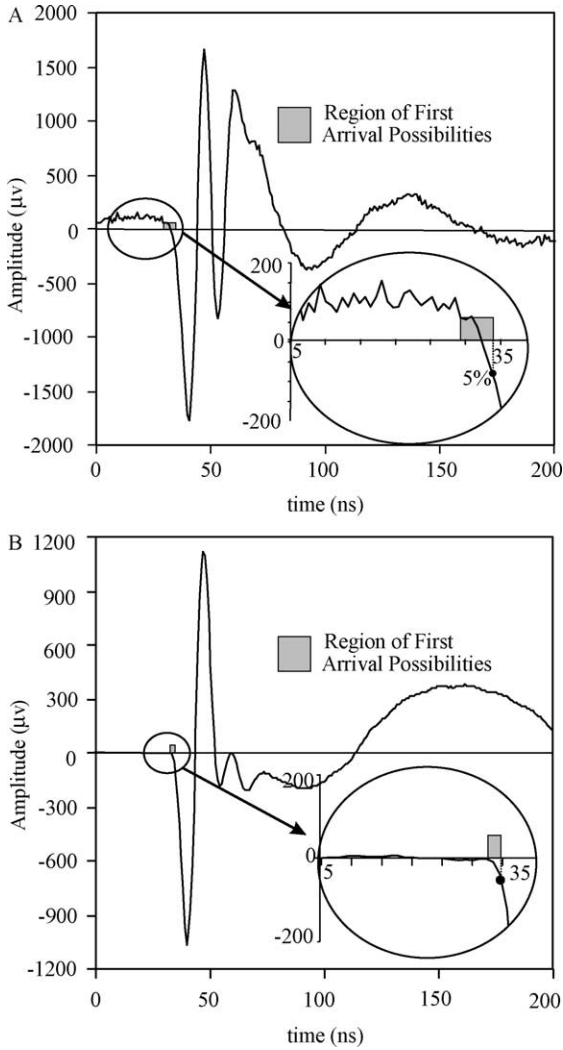


Fig. 2. (A) Recorded noisy trace of a radar pulse at the West Campus Agricultural Center, in Tucson, AZ. Identified on the trace are the first arrival possibilities spanning those found by manual and automated methods. (B) Example of a trace with a low noise including the time pick range.

Equation 19 from Rucker and Ferré (2004a):

$$v_{\text{soil}} = \frac{2v_{\text{air}}}{\sqrt{\left(\frac{dt}{dz}\right)^2 v_{\text{air}}^2 + 4}} \quad (12)$$

where  $dt/dz$  is the slope of the travel time profile (18.33 and 22.98 ns m<sup>-1</sup> for the latest and earliest pick times, respectively). Based on this relationship,

the same range of first arrival times seen in Fig. 2A gives rise to volumetric water content estimates ranging from 0.161 to 0.239 cm<sup>3</sup> cm<sup>-3</sup>.

The preceding demonstrates that the water content uncertainty depends on the travel path of the first arriving energy. In general, the sensitivity of the inferred water content to a change in the travel time for a direct wave calculation can be obtained by substituting Eq. (1), with  $v=v_{\text{soil}}$ , into Eq. (11) then taking the derivative with respect to travel time:

$$\frac{\partial \theta}{\partial t_{\text{direct}}} = 0.1181 \frac{v_{\text{air}}}{x}. \quad (13)$$

Note that Eq. (13) is a constant regardless of the depth of measurement. For an antennae separation,  $x$ , of 3 m, the change in water content due to a 1 ns change in travel time is 0.011 cm<sup>3</sup> cm<sup>-3</sup>. The sensitivity of the inferred water content to the measured travel time for a critically refracted wave can be obtained similarly by substituting Eqs. (2) and (3) into Eq. (11), then taking the derivative with respect to travel time:

$$\frac{\partial \theta}{\partial t_{\text{refr}}} = \frac{\sqrt{\theta^2 + 0.3682\theta + 0.0199}}{\theta + 0.1841} \frac{0.1181 v_{\text{air}}}{2z}. \quad (14)$$

The sensitivity of the water content for a critically refracted wave relies on both the position of the antennae relative to the boundary and the water content of the medium. The sensitivity to errors in the refracted travel time rises steeply as the antennae are placed more closely to the boundary. The sensitivity decreases continuously to a value similar to that associated with direct arrivals at the refraction termination depth. For example, values of  $z$  of 0.25 and 0.5 m and an actual water content of 0.3 cm<sup>3</sup> cm<sup>-3</sup>, the sensitivities of the inferred water contents to a 1 ns change in travel time are 0.07 and 0.035 cm<sup>3</sup> cm<sup>-3</sup>, respectively. When  $z$  is equal to  $z_{\text{rtld}}$  (1.169 m), the sensitivity of the water content to the refracted travel time is 0.015 cm<sup>3</sup> cm<sup>-3</sup>.

#### 2.4. Inverse model

Inversion of the data kernel matrices of Eqs. (5) and (8) to solve for the model parameters is

straightforward, provided that the first arrival travel time path is known with certainty or that  $\mathbf{T}$  is known. Field measurements with BGPR provide only the travel time profile,  $\mathbf{t}$ , which represents one entry per row of the travel time matrix. Inversion of Eq. 2 with  $\mathbf{t}=\mathbf{d}$  is ill-posed because  $\mathbf{G}$  is not known with certainty. To overcome this difficulty, a series of forward models can be run with different velocity (or slowness) values to determine their first arrival travel time profiles. The modeled travel time profile can be compared to the measured travel time profile to identify the velocity profile that reduces the sum of the squares of the differences between the travel times at all depths. The inverse problem can be solved iteratively provided that a method is devised to iteratively change the velocity profile for each iteration in a manner that reduces the travel time misfit. For our problem, we chose the direct velocity as the starting model, since many measured ZOP BGPR travel times are typically associated with direct waves. For the optimization, we chose simulated annealing, which randomly perturbs the velocity and accepts, with a probability of 1, a better fit solution and accepts with a probability less than 1 a worse fit solution. Many possible optimization approaches could have been applied to this inverse problem. We chose simulated annealing despite the fact that it is slow to reach an optimal solution. However, since it is a stable optimization method, it is well suited to the analysis of BGPR travel time profiles.

The objective of the optimization was to minimize the energy,  $E(\mathbf{v})$ , where:

$$E(\mathbf{v}) = \sqrt{\sum_{j=1}^N [t_f(l_j) - \hat{t}_f(l_j, \mathbf{v})]^2}, \quad (15)$$

and  $\mathbf{v}$  represents an EM velocity trial vector to model the first arrival travel time,  $t_f$  is the measured first arrival travel time in each layer  $l_j$ ,  $\hat{t}_f$  is the numerically modeled first arrival travel time given the trial vector  $\mathbf{v}$  and  $N$  is the total number of layers.

### 2.5. Global optimization with simulated annealing

Simulated annealing is a global optimization method that mimics the behavior of a slow cooling solid in a heated bath (van Laarhoven, 1988;

Otten and van Ginneken, 1989; Aarts and Korst, 1989). To simulate the annealing process for our optimization problem, a random-walk model was devised that perturbs the velocities in a random direction by a random amount. A velocity model that improves the fit (decreases the objective function defined in Eq. (15)) from iteration  $i$  to iteration  $i+1$  is accepted. A velocity model that worsens the fit is accepted according to the Metropolis algorithm (Salamon et al., 2002):

$$\Pr\{\text{accept } i+1\} = \begin{cases} 1 & \text{if } E(i+1) \leq E(i) \\ e^{(-\frac{\Delta E}{c})} & \text{if } E(i+1) > E(i) \end{cases} \quad (16)$$

where  $\Delta E = E(i+1) - E(i)$  and is the difference between the new energy state and the current energy state,  $c$  is the control parameter, and  $e^{(-\frac{\Delta E}{c})}$  is the ‘Metropolis criterion’. The control parameter plays the role of the temperature and is reduced during the course of the simulation following a cooling schedule (Otten and van Ginneken, 1989).

The advantage of simulated annealing is the ability to hill-climb along the error surface, which allows the possibility to escape from local minima (Otten and van Ginneken, 1989). The acceptance of a worse fit depends on the generation of a random number and the separation of the newly proposed energy state to the current energy state. If accepted, the new energy state becomes the current energy state and the process is repeated until a predetermined number of iterations have been completed or until the energy has reached a user-defined minimum value that is not necessarily zero. Through several trials, it was determined that a low energy state of 0.01 was achievable within a reasonable number of iterations.

### 3. Travel-time inversion

Two examples are presented to demonstrate the procedure by which simulated annealing is used to find the water content profile. The first example inverts the first arrival travel time data obtained from a forward model of a simple half space with a known soil velocity of 0.1 m/ns. This example shows the outcomes of inversion with and without error in

the first-break pick. The travel time uncertainty is presented through the use of a travel time misfit allowance when fitting the modeled travel time to the measured travel time. The misfit allowance is the absolute maximum travel time within each layer by which the model is allowed to differ from the measured travel time, and represents the energy,  $E(y,N)$ , used in the objective function. The second example inverts first arrival travel time data collected before and after an infiltration experiment at the Western Campus Agricultural Center (WCAC) in Tucson, AZ. The before- and after-infiltration travel time measurements incorporate the first-break pick errors by individually picking the upper and lower bounds of the likely first arrival travel time for each trace. The midpoint of this range is used as the measure of fitness to compare with the modeled travel time and the endpoints define the travel time uncertainty.

### 3.1. Half-space model

The conceptual model for the half-space example is presented in Fig. 3A. The datum is located at the ground surface, and the  $z$ -axis extends positive downwards. The forward model of the first arrival travel time assumes that ZOP BGPR data are collected every 0.25 m, starting at 0 m and extending to 2.25 m bgs. The antennae separation is 3 m. As discussed in Rucker and Ferré (2003), the refraction termination depth for the two velocities used in this model is 1.06 m. Therefore, the first four travel time measurements made beneath the ground surface are derived from critically refracted first arrivals, while the first measurement (in air) and the last five measurements are from direct first arrivals. The first arrival travel time profile is shown in Fig. 3B. For the inversion algorithm, each measurement is assumed to be made from within a discrete layer, separate from

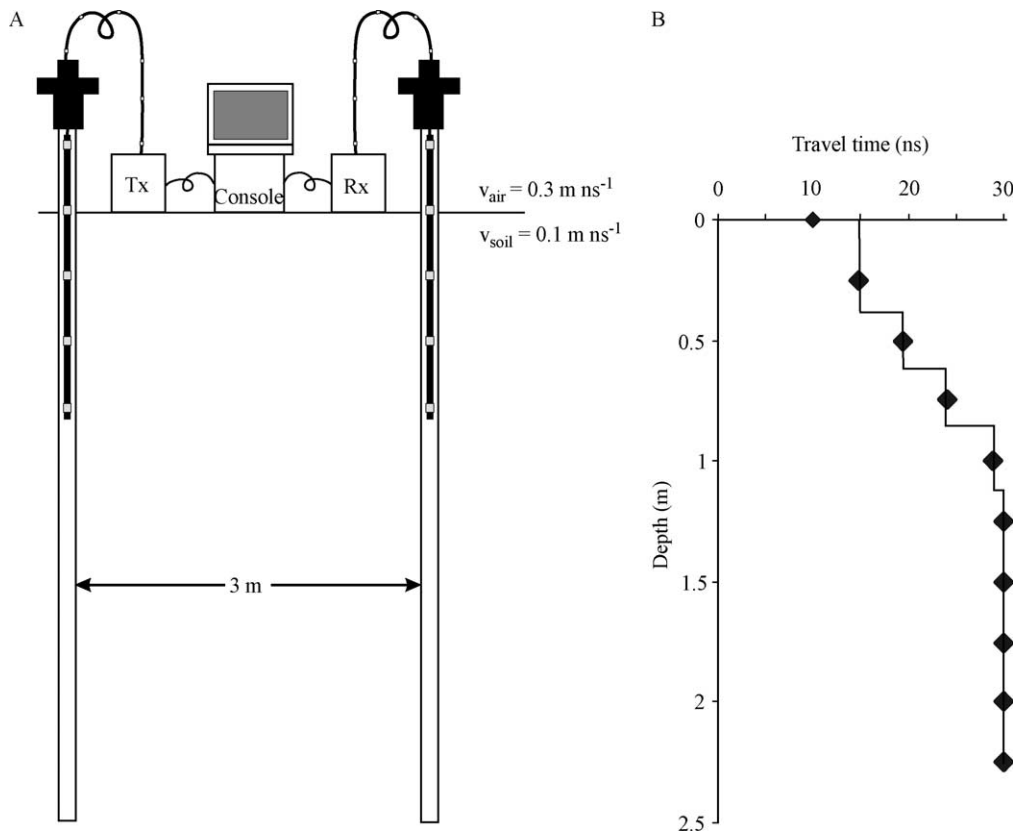


Fig. 3. (A) Conceptual model of a half-space. (B) Calculated travel time profile for the half-space.

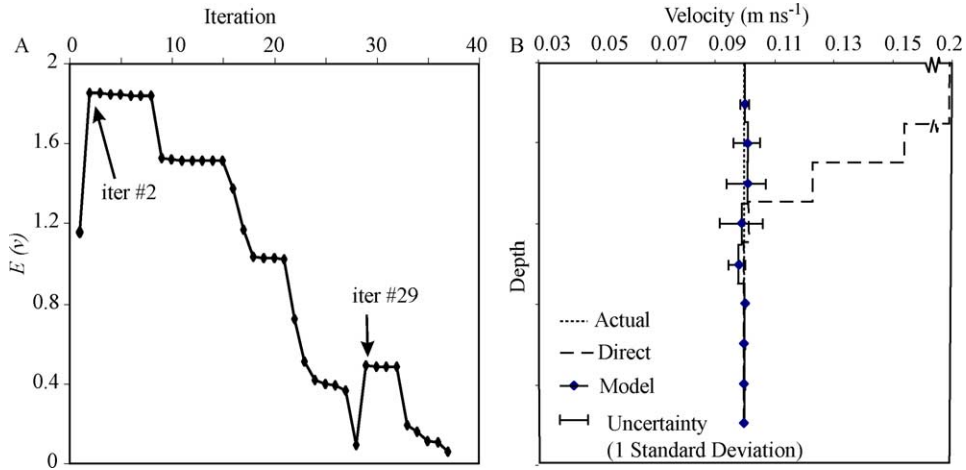


Fig. 4. (A) Value of the objective function during simulated annealing optimization. (B) Ensemble statistics from 960 Monte Carlo realizations from simulated annealing optimization. The uncertainty is represented by one standard deviation. The known velocity and velocity computed assuming direct—only arrivals are shown for reference.

the adjacent layers. The boundaries between the layers are located midway between the travel time measurements, giving the travel time profile of Fig. 3B a discontinuous appearance.

The inversion results for the error-free half-space can be seen in Fig. 4. A travel time misfit allowance was set to 0.4 ns, and smoothing was implemented by minimizing both the first and second derivative. For the mechanics of incorporating the regularization procedure, the reader is referred to Rucker and Ferré (2004b). For this analysis, a Monte Carlo approach was adopted, whereby a large number of individual velocity models (realizations) were generated. The search for the lowest energy state takes a different path during each realization due to the methodology of perturbing and accepting the velocity within an individual layer. Therefore, the proposed velocity model could be different from one realization to the next, and the ensemble statistics are generated from the set of successfully completed realizations (those that complete within the allotted user-specified iterations). For our Monte Carlo simulations, each velocity model has an equal probability of being correct.

A total of 960 Monte Carlo realizations of 1000 attempted were successfully completed within 100 iterations. A realization is unsuccessful if the energy state does not fall below the minimum energy state designated by the user, and is usually the result of a previously modeled layer being fitted at the extreme

values of the uncertainty range in the travel-time pick. Fig. 4A shows the value of the objective function during one of the successful realizations. The average number of iterations needed to complete the simulation was 34. Fig. 4A shows two regions (iterations #2 and #29) where a higher energy value than the energy of the preceding iteration was accepted. Fig. 4B shows the resultant velocity model for the inversion. The solid line represents the ensemble mean from the successfully completed realizations. The error bars represent one standard deviation of the ensemble. The model matched the actual velocity profile quite well. The difference between the mean velocity profile and the actual profile differed by no more than one standard deviation. As a comparison, the profile assuming that all arrivals are direct arrivals is shown to differ greatly from the actual velocity profile.

When making a first-break pick, both human and instrument error are combined to form the total picking error. The uncertainty range in first-break picking is an example of human error, where judgment is used to locate the first arrival travel time. The absolute difference between the midpoints of the time range to the real travel time can be categorized as instrument error, representing statistically random error of the time-zero pick. To examine the nature of these errors, 80 traces measured in air were selected from approximately 1.5 years of data collection at WCAC, in Tucson, AZ. A Sensors and

Software (Mississauga, Canada) GPR system with 100 MHz borehole antennae was used for all measurements. The ranges for all 80 picks are shown in Fig. 5A. The known travel time in air ( $x/v_{\text{air}} = 10.833$  ns) is also plotted. Early and late time picks for each trace were obtained using the manual and automatic methods described above. The machine error can be defined as the difference between the midpoint of the range and the correct time. The machine error was normally distributed (Fig. 5B) with a mean error (bias) of 0.451 ns.

The average range in the first-break picks was 1.4 ns (Fig. 5C), representing the first-break pick uncertainty. This range, however, only represents the traces in air at the WCAC. As seen in Fig. 2A and B, different circumstances can produce a different set of ranges, depending on the level of noise present, the amount of attenuation, and the sampling resolution. In general, it is not suggested that a standard range in the first-break pick be used to obtain the level of confidence of calculated water content. Ideally, the range should be evaluated individually for each trace.

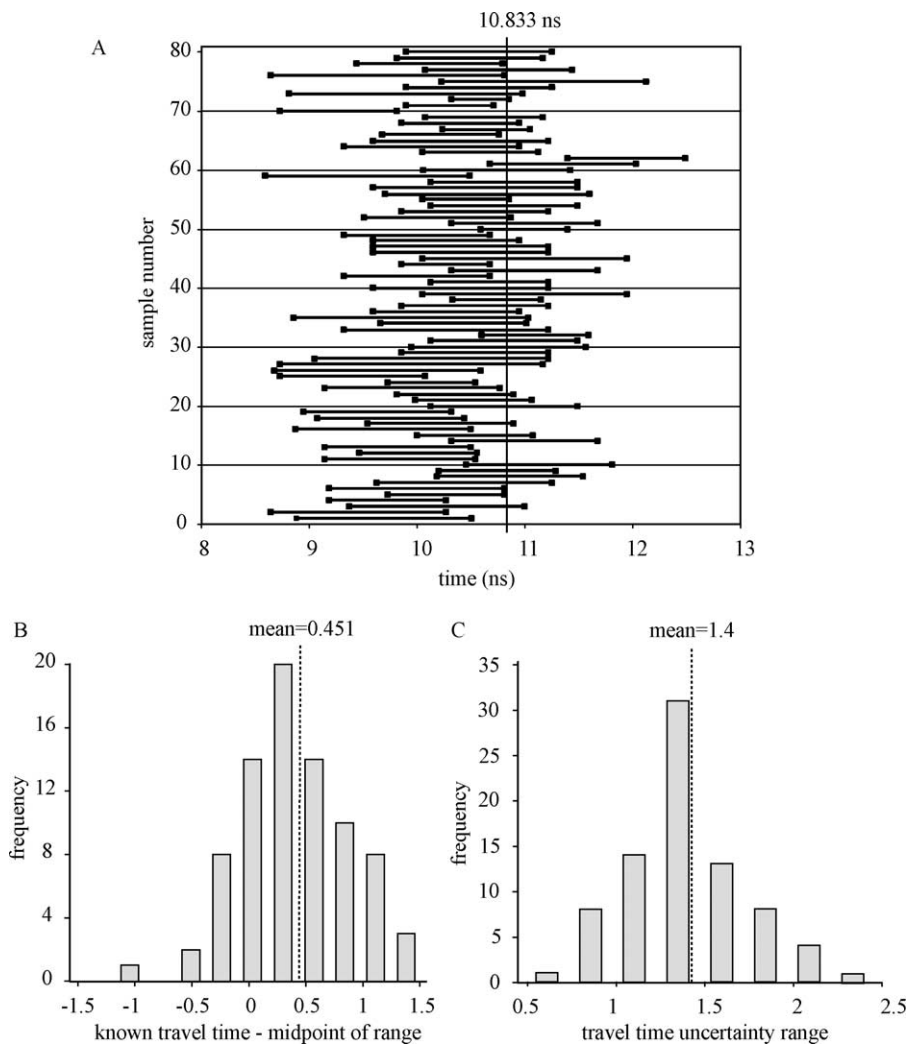


Fig. 5. (A) Ranges of possibilities for first arrivals obtained from 80 traces in air with an antennae separation of 3.25 m. The actual travel time should be 10.8333 ns. (B) A histogram of the difference between the actual travel time and midpoint of the range from 80 traces in air. (C) A histogram of the travel time uncertainty range from 80 traces in air.

In situations where travel time profiles contain a single, best-guess first-break pick for each measurement, a constant travel time uncertainty may be necessary. However, the uncertainty should be large enough to capture the relevant noise that may be present in the original data.

To test the effects of picking error on the uncertainty of the interpreted water content profile, random noise was added to the first-break picks for the half-space model. The error was derived from a normal distribution with a mean of 0 ns. Fig. 6 shows the resultant water content profile after modeling with

the simulated annealing algorithm. The travel time profile of Fig. 6A was generated by adding a normal error with standard deviation of 0.5 ns. No smoothing was applied to the data in Fig. 6A. The results show that there is a strong oscillation in water content in regions of critical refraction. However, the small uncertainty in the final set of completed realizations shows that the algorithm converged to the same final model in almost every run. The first arrival travel time for the first measurement (at 0.25 m bgs) increased from 14.7 ns for the error-free to 15.3 ns with error. The travel time increase forced the solution to fit

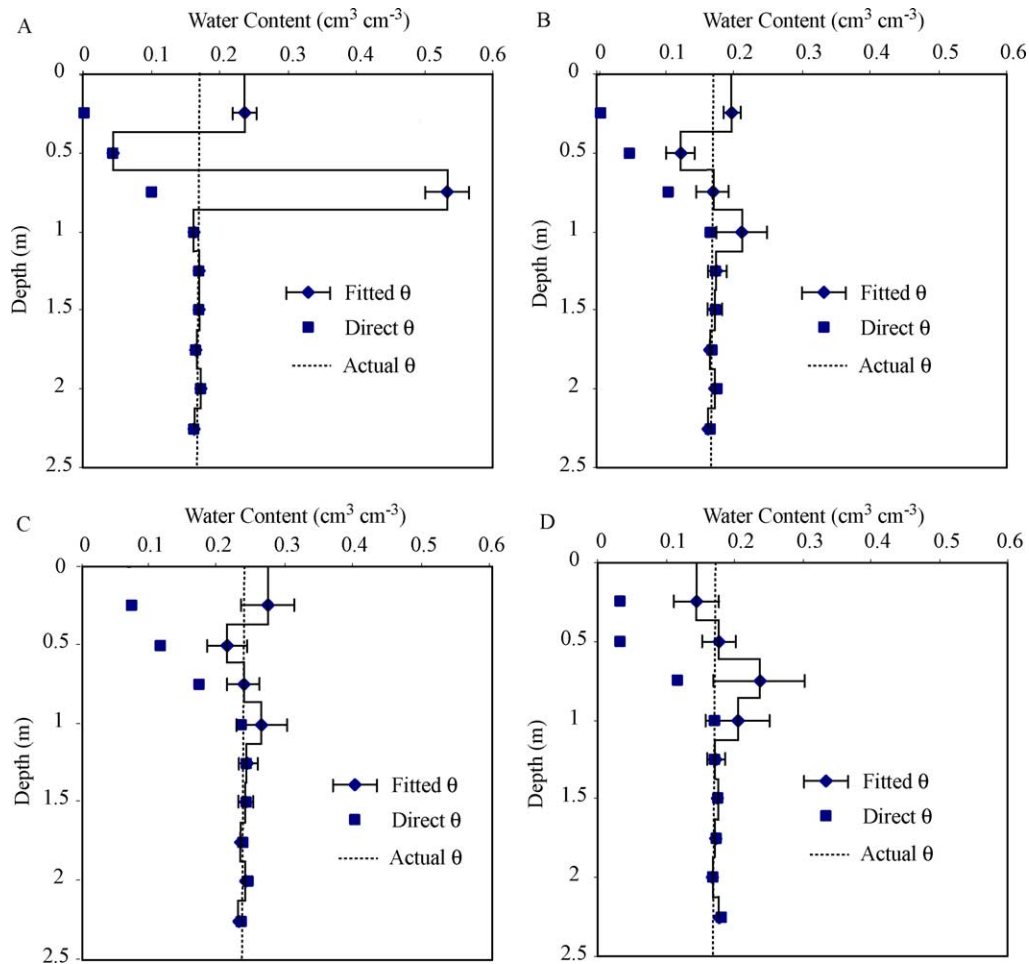


Fig. 6. Water content models of half space from noisy travel time data. (A) Noise from a normal distribution with a mean of 0 ns and standard deviation of 0.5 ns. The inversion included no smoothing. (B) Same as (A), but with smoothing through minimization of the first and second derivative. The travel time misfit allowance is smaller than the degree of noise. (C) Same as (B), but with larger misfit allowance, which increases the water content uncertainty. (D) Noise from a normal distribution with a mean of 0 ns and standard deviation of 1 ns, smoothing, and misfit allowance larger than the degree of noise.

a smaller velocity, thus increasing the water content. Each subsequent velocity had to compensate for the first velocity creating the observed oscillations. For comparison, the water content of an assumed direct velocity model is also plotted in Fig. 6. The simulated annealing solution shows that the measurement made 0.5 m bgs with a measured travel time just 0.1 ns less than the error-free values was forced to be a direct travel time from overcompensation from the first fitted velocity.

The degree of oscillations was dampened in Fig. 6B, wherein moderate smoothing was used in the solution and a travel time misfit allowance of 0.4 ns was applied. As described in Rucker and Ferré (2004b), smoothing is applied through minimization of the first and second derivative and moderate smoothing is defined as having the first derivative less than 0.033 m/ns and a second derivative less than 0.066 m/ns.

The solution in Fig. 6B continues to show a deviation from the true water content and the range of uncertainty of a few layers do not overlap the region of the true water content. This is probably due to the restrictive use of a maximum travel time misfit allowance that is smaller than the degree of the travel time error. Fig. 6C shows that when the maximum travel time misfit allowance is less restrictive, i.e. larger than the added first-break picking error, the true water content is within the uncertainty of the model. Lastly, Fig. 6D, computed from a travel time profile containing a picking error with a standard deviation of 1 ns, shows that as the error in first break picks increases, the final water content can deviate drastically from the actual solution. However, the solution is still improved over the solution assuming that all first arrivals are direct.

### 3.2. Field measurements

An infiltration experiment was conducted at a field site located at the WCAC. ZOP BGPR travel time measurements were taken before infiltration began and after infiltration ceased. The infiltration occurred within a bermed infiltration gallery with square dimensions of 5 m × 5 m (Rucker and Ferré, 2003). Water was applied at the surface through a manifold that distributed the water evenly over the area at a constant rate of  $9.44 \times 10^{-5} \text{ m}^3 \text{ s}^{-1}$  for 66 h. This

infiltration rate was chosen to minimize ponding at the surface. Two-inch, PVC-cased boreholes were completed to 15 m within the gallery. The borehole separation was 3.25 m.

A soil profile was characterized by inspection of continuous cores obtained during drilling of the boreholes. The top 15 cm of soil consists of dry, unconsolidated loose sand and silt. A thick (~3.3 m) sandy layer with interspersed lenses of organic material and clay underlies the surface material. A black, peat-like organic layer is located approximately 1 m below surface. The material between 3.3 and 6.5 m depth is a gravely sand, which grades to cobbles, gravel, and sand to 8.5 m. From 8.5 to 13 m the medium varies from a 1.5 m-thick clay lens to a clayey sand. The remainder of the profile to 15 m is comprised of fine sand with small amounts of clay.

The sampling discretization interval for the ZOP BGPR was 0.25 m. Fig. 7A and B shows the travel time profiles before and after infiltration. The profiles were generated using the upper and lower limit of the first arrival travel time for each trace based on the manual and automatic methods described above. The symbols demarcate the mean travel time at each depth. The mean travel time pick was shifted to the right by approximately 0.45 ns and the first measurement was set to the travel time of an EM wave in air. The shift was determined by subtracting the known travel time in air from the first-break pick in air. These shifts accommodate the bias in the manual first break picking compared to the automated picker for finding time-zero and random machine error.

Parts of the profile show greater confidence (smaller range) in the first break pick than others. These first-break picks are in regions where clay content is at a minimum. The clay, which has a high electrical conductivity, attenuates the pulse, adding uncertainty to the first break picking. Increased water contents following infiltration also leads to higher electrical conductivity, which causes the picking errors to increase slightly after infiltration. This is particularly evident at the edge of the wetting front, located from about 5.25 to 5.5 m bgs. The uncertainty in first-break picks increases from 0.42 ns above the wetting front to 1.98 ns at the wetting front.

The WCAC travel time profiles were analyzed using the simulated annealing algorithm with the same parameters used in the base case of

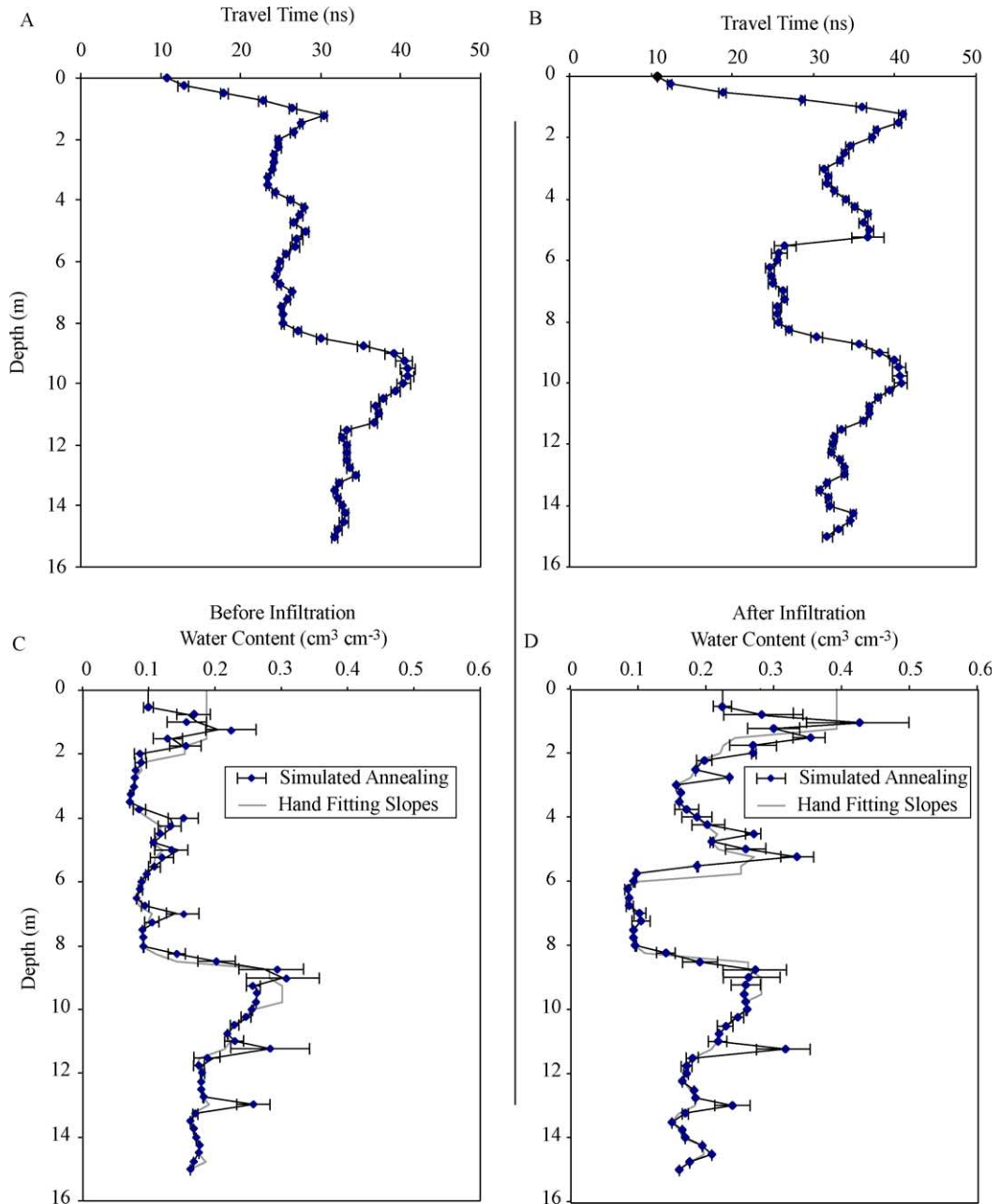


Fig. 7. Travel time measurements (A) before and (B) after a field infiltration experiment. Calculated water content after simulated annealing algorithm from (C) before and (D) after infiltration. Hand-fitted slopes from (Rucker and Ferré, 2003a) are included for comparison.

the half-space model, including moderate smoothing. The maximum travel time misfit allowance was evaluated separately for each trace based on the first break picking uncertainty. The simulations were run

with 1000 Monte Carlo realizations to obtain an ensemble mean and range in velocity and water content uncertainty. Fig. 7C and D shows the interpreted water content from the fitted velocity

model using Eq. (11). Note that areas of high water content also have larger uncertainties. This is due mainly to the higher likelihood that critical refractions will be first arriving in these regions. Conversely, areas within the profile that contain direct first arrivals have small uncertainties.

Fig. 7C and D includes a water content profile derived from hand fitting slopes to the linearly increasing/decreasing portions of the travel time profile, as presented in Rucker and Ferré (2003; 2004a). The two methods for determining water content show slight disagreement, especially in regions of critical refraction. Within the top 2 m near the ground surface, for example, the hand-fitted slope method produces a constant water content of approximately  $0.17 \text{ cm}^3 \text{ cm}^{-3}$ . The slope method relies on all measurements in regions of increasing travel time and cannot distinguish between individual travel time measurements within the region experiencing critical refraction. Deviations in travel time along the linear slope are considered to contribute to a single error during the regression analysis. Additionally, the location of the layer boundaries caused some differences in the two methods. The boundary was presumed to be located at the measurement location for the slope method, whereas for the automated fitting with simulated annealing, the boundary was located between measurements. The latter forced some regions to be interpreted to have critically refracted first arrivals in the simulated annealing profile and direct arrivals in the slope method (e.g. 11.5 and 13 m bgs). To help locate boundaries with greater precision, a higher sampling rate is needed. A higher rate reduces the effects of spatial aliasing, which occurs because the measurement interval is too large compared to the stratigraphic layer thickness.

Following the approach of Rucker and Ferré (2003), comparison of the measured total length of water added to the upper 6 m ( $\Delta L_w$ ) during infiltration with the known amount of water added at the surface was used as a performance measure of the simulated annealing analysis. The length of water ( $L_w$ ) was calculated by numerically integrating the water content over the top 6 m, assuming that the water content is constant within each layer. The 6 m cut-off was considered to be the maximum extent to which water infiltrated during the 66-h experiment. Rucker and Ferré (2004a) reported the slope method having

a computed  $\Delta L_w$  of 0.81 m, compared to the applied amount of 0.898 m. The after infiltration  $L_w$  was computed to be 1.39 m, and the before infiltration  $L_w$  was computed to be 0.64 m for the automated fitting model with simulated annealing. This results in a value of  $\Delta L_w$  of 0.75 m, which is comparable to the applied water. The uncertainty range in water content of each layer allowed the computation of the uncertainty in  $L_w$ . The maximum  $\Delta L_w$  was computed by taking the difference between the upper end of the water content for the after-infiltration profile and the lower end of the before infiltration profile. The converse was applied for the minimum  $\Delta L_w$ . The minimum and maximum change in total water length were 0.51 and 0.89 m. Although the  $\Delta L_w$  from the graphical solution was closer to the length of water applied at the surface than the mean solution from the automated inversion, no level of confidence can be computed for the graphical solution.

#### 4. Discussion and conclusion

To overcome the difficulty of direct inversion for velocity (and eventually water content), a global optimization routine was developed, whereby a starting velocity model was perturbed randomly and a forward model was solved to determine the first arrival travel time profile. The objective was to minimize the difference between the modeled and measured travel time profiles. The routine incorporated simulated annealing, which uses various aspects of random-walk iterative improvement and blind random search (Otten and van Ginneken, 1989) to help find the global minimum of the error surface (the ground energy state). By using the Metropolis criterion to accept with non-zero probability worse fits to the velocity model, local minima are avoided.

The correct maximum travel time misfit allowance and the inclusion of smoothing constraints were important in properly assessing the water content profile. The maximum travel time misfit allowance provides some margin of error during the fitting of a randomly derived velocity model. A maximum travel time misfit allowance that is too small may affect the solution in terms of (1) longer run time and (2) overconstraining the solution, i.e. fitting too tightly to measurements that could be prone to error.

In the latter case, the remaining velocity values will have to compensate for a fitted velocity that may be incorrect, and the simulation could fail to meet its objective. In some instances, a large maximum travel time misfit allowance may be warranted from the resolution of the trace within the radargram, i.e. first-break picks may be difficult to locate with precision. Conceptually, the maximum travel time misfit allowance controls how large the global minimum target will be, with a large maximum travel time misfit allowance flattening the bottom of the error surface.

Regularization through smoothing the velocity model was found to be necessary in the example cases tested. Because the starting model assumes direct arrivals and a critically refracted velocity is always lower than the direct, the model tended towards slowly reducing the velocity until the travel time misfit allowance was met. The fitted velocity had a propensity to remain high for the first layer. The adjacent layer velocity, having to compensate for the high velocity of the first layer, was fit towards the lower end of the velocity range. This successive over compensation manifested itself throughout the remaining profile, causing oscillations between high and low values in several of the final velocity models. To minimize the effects of an oscillating velocity model, the smoothing criteria forced three velocity layers to be perturbed at once in the same direction. Additionally, reducing the maximum travel time misfit allowance helped minimize oscillations because the number of possible solutions to the velocity model decreased.

The inferred volumetric water content was shown to be sensitive to the uncertainty in first arrival travel time pick and to depend on the travel path of the first arriving energy. Uncertainty in the travel time pick arose from both instrument and human error. The instrument error was characterized by the bias of the instrument during calibration, and was evaluated by comparing the midpoint in the range of the author's first-break picks of traces in air (known velocity) at a known separation. It is assumed that the bias is constant throughout the short collection time of a single profile, even though it has been known to drift over extended periods of use (Hubbard, 2002). To compensate for bias, it may be necessary to adjust the travel time of a measurement in air to be the correct value and subsequently adjust the remaining travel

times deeper in the profile by this amount. Others (Ferré et al., 2003) have reported adjusting first arrival travel times based on a measurement that should remain constant in a time series of profiles (e.g. below the water table). Human error in first-break picks was evaluated by comparing the possible range of first arrival travel time picks for a trace, which can be obscured by noise, attenuation, and resolution. The human picking error is not constant and can vary throughout a profile.

Stochastic parameter estimation using the Monte Carlo method is a popular method to quantify model uncertainty in hydrologic applications, for example the extent of capture zones around a well (Feyen et al., 2001; Vassolo et al., 1998). For the present analysis, we used the Monte Carlo method to quantify the uncertainty on the inversion estimates of EM wave propagation velocity, and finally water content, from measurements made of first-break picks in ZOP BGPR surveys. The definition of our objective function precluded the use of a covariance matrix and all measurements were given the same relative importance. It is suggested that if the underlying statistical distribution of a measurement is unknown, and a covariance matrix cannot be calculated, that a Monte Carlo simulation similar to that presented in this paper be performed.

For the synthetic example of a simple half-space, the ensemble mean of the successfully completed realizations was used as a criterion to evaluate the accuracy of the inverted water content model to the known water content profile. The ensemble standard deviation was used arbitrarily to characterize the uncertainty of the inferred water content profile. Other ensemble statistics could have been used, including the minimum and maximum water content. In all of the synthetic examples, when the travel time misfit allowance was larger than the error in travel time pick, the known value of water content fell within our uncertainty range of the inferred water content.

The field measured travel time profiles before and after infiltration were inverted using simulated annealing. The before infiltration case completed all 1000 realizations attempted, whereas the after infiltration case completed only 904. The difficulty occurred at the bottom edge of the wetting front (5.25 m bgs), where the algorithm had difficulty fitting the critically refracted arrival while keeping the

measurement at 5.5 m bgs a direct arrival. In many layers, the water content derived from the hand-fitted slope analysis was either equal to or at least within the range of uncertainty of the automated inversions. Exceptions occur mainly in regions where the slope method could not discern thin low-velocity layers within the profile, for example in the upper 2 m near the ground surface and at the clay layer at roughly 10 m bgs. Since the simulated annealing algorithm can treat each layer independently, higher resolution of water content profile is obtained. Additionally, major differences in the two methods occur at regions where critical refraction may or may not be taking place, due to the unknown location of the boundary and the possibility of spatial aliasing. These regions are located at 11.5 and 13 m bgs in this study. It is difficult to discern whether the first arrival travel time is from a critically refracted or a direct wave, because only one measurement was made within these regions. As it stands, both methods produce a water content profile at these depths with equal likelihood and the uncertainty range could be updated to include both methods. To resolve the issue of spatial aliasing, a higher spatial sampling rate, or smaller sampling interval is needed in regions of critical refraction (Rucker and Ferré, 2004a).

## Acknowledgements

This material is based on work supported by the National Science Foundation under Grant no. 0097171. Additional support was provided by funds from NASA under contract NASA/JPL 1236728.

## References

- Aarts, E., Korst, E., 1989. *Simulated Annealing and Boltzmann Machines*. Wiley, New York.
- Boschetti, F., Dentith, M.C., List, R.D., 1996. Inversion of seismic refraction data using genetic algorithms. *Geophysics* 61 (6), 1715–1727.
- Cai, J., McMechan, G.A., 1995. Ray-based synthesis of bistatic ground-penetrating radar profiles. *Geophysics* 60 (1), 87–96.
- Carrera, J., Neuman, S.P., 1986. Estimation of aquifer parameters under transient and steady state conditions: 1. Maximum likelihood method incorporating prior information. *Water Resources Research* 22 (2), 199–210.
- Davis, J.L., Annan, A.P., 1989. Ground-penetrating radar for high-resolution mapping of soil and rock stratigraphy. *Geophysical Prospecting* 37, 531–551.
- Davis, J.L., Annan, A.P., 2003. Ground penetrating radar to measure soil water content, in: Dane, J.H., Topp, G.C. (Eds.), *Methods of Soil Analysis Part 4—Physical Methods*. Soil Science Society of America, Madison, WI, pp. 446–463.
- Feng, S., Sen, P.N., 1985. Geometrical model of conductive and dielectric properties of partially saturated rocks. *Journal of Applied Physics* 58 (8), 3236–3243.
- Ferré, P.A., Rudolph, D.L., Kachanoski, R.G., 1996. Spatial averaging of water content by time domain reflectometry: implications for twin rod probes with and without dielectric coatings. *Water Resources Research* 32 (2), 271–279.
- Ferré, T.P.A., von Glinski, G., Ferré, L.A., 2003. Monitoring the maximum depth of drainage in response to pumping using borehole ground penetrating radar. *Vadose Zone Journal* (accepted for publication).
- Feyen, L., Beven, K.J., Smedt, F.D., Freer, J., 2001. Stochastic capture zone delineation within the generalized likelihood uncertainty estimation methodology: conditioning on head observations. *Water Resources Research* 37 (3), 625–638.
- Friedman, S.P., 1997. Statistical mixing model for the apparent dielectric permittivity constant of unsaturated porous media. *Journal of Hydrology* 61, 742–745.
- Friedman, S.P., 1998. A saturation degree-dependent composite spheres model for describing the effective dielectric constant of unsaturated porous media. *Water Resources Research* 34 (11), 2949–2961.
- Hubbard, S.S., 2002. Personal Communication.
- Menke, W., 1989. *Geophysical Data Analysis: Discrete Inverse Theory*, Revised Edition ed. Academic Press, Inc., New York.
- Mosegaard, K., Vestergaard, P.D., 1991. A simulated annealing approach to seismic model optimization with sparse prior information. *Geophysical Prospecting* 39 (5), 599–611.
- Otten, R.H.J.M., van Ginneken, L.P.P.P., 1989. *The Annealing Algorithm*. Kluwer Academic Publishers, Dordrecht, The Netherlands.
- Rucker, D.F., Ferré, T.P.A., 2003. Near-surface water content estimation with borehole ground penetrating radar using critically refracted waves. *Vadose Zone Journal* 2 (2), 247–252.
- Rucker, D.F., Ferré, T.P.A., 2004a. Correcting water content measurement errors associated with critically refracted first arrivals on zero offset profiling borehole ground penetrating radar profiles. *Vadose Zone Journal* 3 (1), 278–287.
- Rucker, D.F., Ferré, T.P.A., 2004b. BGPR\_Reconstruct: a MATLAB ray-tracing program for nonlinear inversion of first arrival travel time data from zero-offset borehole radar. *Computers and Geosciences* 30 (4), 767–776.
- Salamon, P., Sibani, P., Frost, R., 2002. *Facts, Conjectures, and Improvements for Simulated Annealing*. SIAM, Society for Industrial and Applied Mathematics, Philadelphia.

- Sensors and Software, 1999. pulseEKKO 100 RUN User's Guide, Version 1.2, Technical Manual 25. Sensors and Software, Inc., Mississauga, ON L4W 3R7 Canada.
- Tabbagh, A., Camerlynck, C., Cosenza, P., 2000. Numerical modeling for investigating the physical meaning of the relationship between relative dielectric permittivity and water content in soils. *Journal of Hydrology* 36 (9), 2771–2775.
- Tikhonov, A.N., Arsenin, V.Y., 1977. *Solutions of Ill-posed Problems*. Wiley, New York.
- Topp, G.C., Davis, J.L., Annan, A.P., 1980. Electromagnetic determination of soil water content: measurements in coaxial transmission lines. *Water Resources Research* 16 (3), 574–582.
- van Laarhoven, P.J.M., 1988. *Theoretical and Computational Aspects of Simulated Annealing*, Stichting Mathematisch Centrum. Centrum voor Wiskunde en Informatica, Amsterdam.
- Vassolo, S., Kinzelbach, W., Schafer, W., 1998. Determination of a well head protection zone by stochastic inverse modelling. *Journal of Hydrology* 206 (3–4), 268–280.